Testing a polarimetric cloud imager aboard research vessel *Polarstern*: comparison of color-based and polarimetric cloud detection algorithms

András Barta,[1,2,5] Gábor Horváth,[1,*] Ákos Horváth,[3,6] Ádám Egri,[1,2,7] Miklós Blahó,[1,8] Pál Barta,[2,9] Karl Bumke,[4,10] and Andreas Macke[3,11]

[1]Environmental Optics Laboratory, Department of Biological Physics, Eötvös University, H-1117 Budapest, Pázmány sétány 1, Hungary

[2]Estrato Research and Development Ltd., H-1121 Budapest, Mártonlak utca 13, Hungary

[3]Leibniz Institute for Tropospheric Research, D-04318 Leipzig, Permoserstrasse 15, Germany

[4]GEOMAR Helmholtz Centre for Ocean Research, D-24148 Kiel, Wischhofstrasse 1-3, Germany

[5]e-mail: bartaandras@gmail.com

[6]e-mail: akos.horvath@tropos.de

[7]e-mail: adamp39@gmail.com

[8]e-mail: majkl2000@gmail.com

[9]e-mail: pbarta@estrato.hu

[10]e-mail: kbumke@geomar.de

[11]e-mail: andreas.macke@tropos.de

*Corresponding author: gh@arago.elte.hu

Received 10 September 2014; revised 14 December 2014; accepted 15 December 2014; posted 22 December 2014 (Doc. ID 222754); published 5 February 2015

Cloud cover estimation is an important part of routine meteorological observations. Cloudiness measurements are used in climate model evaluation, nowcasting solar radiation, parameterizing the fluctuations of sea surface insolation, and building energy transfer models of the atmosphere. Currently, the most widespread ground-based method to measure cloudiness is based on analyzing the unpolarized intensity and color distribution of the sky obtained by digital cameras. As a new approach, we propose that cloud detection can be aided by the additional use of skylight polarization measured by 180° field-of-view imaging polarimetry. In the fall of 2010, we tested such a novel polarimetric cloud detector aboard the research vessel *Polarstern* during expedition ANT-XXVII/1. One of our goals was to test the durability of the measurement hardware under the extreme conditions of a trans-Atlantic cruise. Here, we describe the instrument and compare the results of several different cloud detection algorithms, some conventional and some newly developed. We also discuss the weaknesses of our design and its possible improvements. The comparison with cloud detection algorithms developed for traditional nonpolarimetric full-sky imagers allowed us to evaluate the added value of polarimetric quantities. We found that (1) neural-network-based algorithms perform the best among the investigated schemes and (2) global information

1559-128X/15/051065-13$15.00/0

(the mean and variance of intensity), nonoptical information (e.g., sun-view geometry), and polarimetric information (e.g., the degree of polarization) improve the accuracy of cloud detection, albeit slightly.

OCIS codes: (010.1615) Clouds; (010.3920) Meteorology; (100.2960) Image analysis; (110.5405) Polarimetric imaging; (280.4991) Passive remote sensing.

http://dx.doi.org/10.1364/AO.54.001065

1. Introduction

Cloud cover is a routine meteorological observation, which can be used in parameterizing the fluctuations of sea surface insolation [1] for nowcasting solar radiation in the management of solar power plants [2] and validating climate models if long time series are available [3]. Ground-based estimates of cloudiness were traditionally obtained by human observations, which, however, were subjective, relatively coarse (given in octas), infrequent, and expensive. The appearance and rapid spread of compact digital cameras made it possible to develop low-cost automated cloud cameras, which can provide an alternative dataset of objective and quantitative cloud cover estimates based on the measured intensity and color distribution of the sky.

A large number of photometric sky imagers are now available on the market, such as (1) Total Sky Imager (Yankee Environmental Systems); (2) Whole Sky Imager (Scripps Institute of Oceanography), and (3) All Sky Imager (Atmospheric Physics Group [4]) just to mention a few. All current sky imagers use nonpolarimetric information (e.g., color) for cloud detection.

As a new approach, we propose that clouds might be better detected from the ground with the additional use of skylight polarization measured by 180° field-of-view imaging polarimetry [5,6].

As confirmed by ground-based polarimetric measurements of the downward directed light field at the bottom of the atmosphere, the celestial distribution of the angle of polarization α exhibits a very robust pattern, which, qualitatively, is the same under all possible sky conditions. The only difference among clear [7,8], partly cloudy [8–10], totally overcast [6], foggy [10], smoky [11], and tree-canopied [12] skies occurs in the degree of linear polarization p: the higher the optical thickness of the nonclear atmosphere, the lower the p-value. The robust behavior of the angle of polarization is due to the predominant role of single scattering, which controls α, even in multiple scattering situations, e.g., under clouds or fog. The degree of polarization p, on the other hand, is more sensitive to the type and size of particles and, thus, might be used to improve cloud detection [13]. The theory and measurement of sky polarization under clear and cloudy conditions, including its expected patterns due to scattering (Rayleigh, clouds, and aerosols) and gaseous absorption, are reviewed in [13–15].

The use of polarimetric information in cloud property retrievals was pioneered by the satellite-borne POLDER (Polarization and Directionality of the Earth's Reflectances) and PARASOL (Polarization and Anisotropy of Reflectances for Atmospheric Sciences with Observations from a Lidar) instruments [16,17]. Such space-based polarimetric measurements are routinely used to distinguish water clouds from ice clouds [15] and determine the effective radius of cloud droplets [18]. In contrast, ground-based polarimetric measurements are mainly used to retrieve the size distribution of aerosols [19], but their application for cloud property retrievals is still in its infancy.

In autumn 2010, we tested a newly developed imaging polarimetric cloud detector aboard the research vessel *Polarstern* during the trans-Atlantic expedition ANT-XXVII/1. Here, we describe our instrument and discuss its weaknesses and possible improvements. The obtained measurement data were processed with a suite of cloud detection algorithms, which included the most frequently used color-based schemes previously developed for traditional full-sky imagers as well as new schemes that take advantage of polarimetric information. Although the considered algorithm suite was not exhaustive, it was sufficiently representative to allow the comparative evaluation of polarimetric and nonpolarimetric methods.

2. Materials and Methods

A. Expedition ANT-XXVII/1

Performing measurements on the *Polarstern* allowed us to sample different climatic regions and compare the results of the different cloud detection algorithms under sky conditions with highly varying cloud coverage. Furthermore, we could test the durability of our cloud detector under the extreme environmental conditions of a trans-Atlantic voyage.

The ANT-XXVII/1 expedition [20] of the research vessel *Polarstern* [Fig. 1(a)] transected the Atlantic Ocean from Bremerhaven, Germany, to Cape Town, South Africa, via Gran Canaria, Canary Islands, between 25 October and 26 November 2010 [Fig. 1(b)]. The first week of the expedition experienced stormy weather in the Bay of Biscay, preventing the installation of our cloud detector. After leaving the stormy zone, we successfully mounted the cloud detector on the upper deck of the ship on 2 November. The cloud detector was working for 15 consecutive days after installation and provided an ample amount of test data.

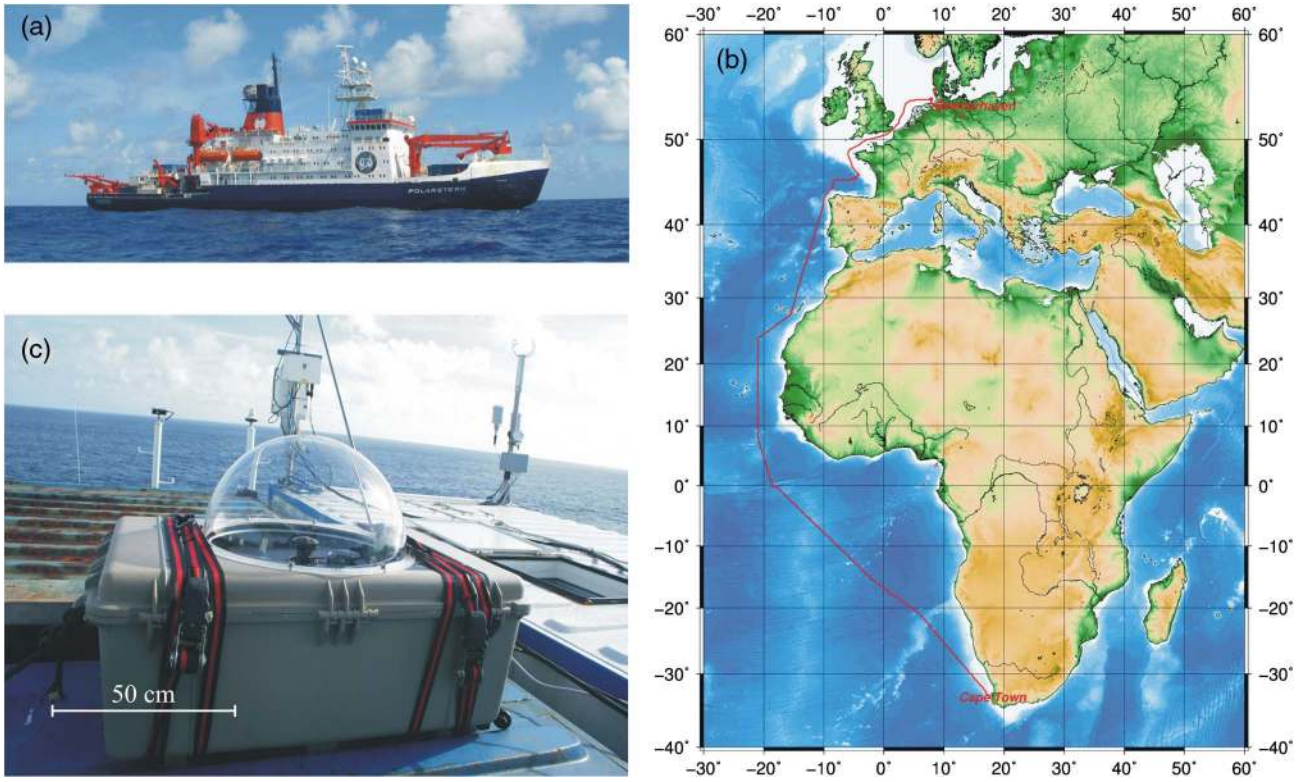

Fig. 1. (a) Research vessel *Polarstern* photographed by Karl Bumke during the ANT-XXVII/1 trans-Atlantic expedition. (b) The route of the expedition from Bremerhaven, Germany, to Cape Town, South Africa, via Gran Canaria, Canary Islands, between 25 October and 26 November 2010 (source: http://www.awi.de/fileadmin/user_upload/MET/PolarsternExpeditionMaps/ANT-XXVII-1.png). (c) Our imaging polarimetric cloud detector installed on the "monkey deck."

B. Full-Sky Imaging Polarimeter

Our polarimetric cloud detector is a portable, single-camera, rotating-analyzer imaging polarimeter. It consists of an industrial digital camera, a 180° field-of-view fisheye optics, a rotating filter wheel with embedded polarizing filters, a sun shield mechanism, an embedded controller, and a weather-proof casing. The internal structure of the cloud detector is shown in Figs. 1(c) and 2. The camera (Imaging Source DFK 41BU02) has a 1280 × 960 pixels resolution 1/2 in. format CCD (Sony ICX205AK) with a Bayer filter that allows near-infrared measurements. The sensitivity spectrum of the CCD is shown in Fig. 3(a). The full sky-dome is mapped onto a circular area of the CCD by a Fujinon FE185-C046HA-1 180° field-of-view fisheye lens. The optical axis of the lens was somewhat misaligned with regards to the center of the CCD, resulting in a small portion of the measurement area being nonutilized (black data void areas in the sky images). The computational method used to extract polarization information from the three full-sky pictures taken through linear polarizers with different directions of their transmission axis has been described in [5,6,15,21].

The disturbing reflection of intense direct sunlight from the internal surfaces of the optical elements was eliminated using a sun occultor, which shaded the lens from direct sunlight. The Mueller matrix of the fisheye lens was measured, as in [5,21]. We found the influence of lens reflections on the polarization state of incident light negligible. Essentially, the same imaging-polarimetric instrument was used in a previous study to successfully measure the polarization transition between sunlit and moonlit skies [22].

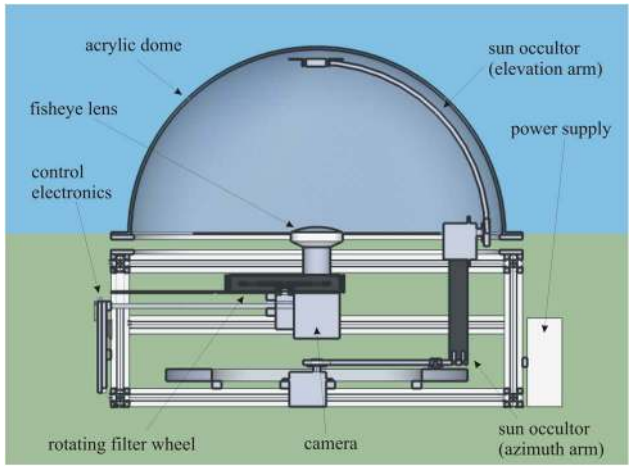

Fig. 2. Cross section of our cloud detector showing its internal structure. The rotating filter wheel between the fisheye lens and the CCD camera contained five filters, as described in Table 1. The independently controllable azimuth and elevation arms of the sun occultor allowed moving the occultor to any position of the acrylic dome to completely shade the fisheye lens from direct sunlight.

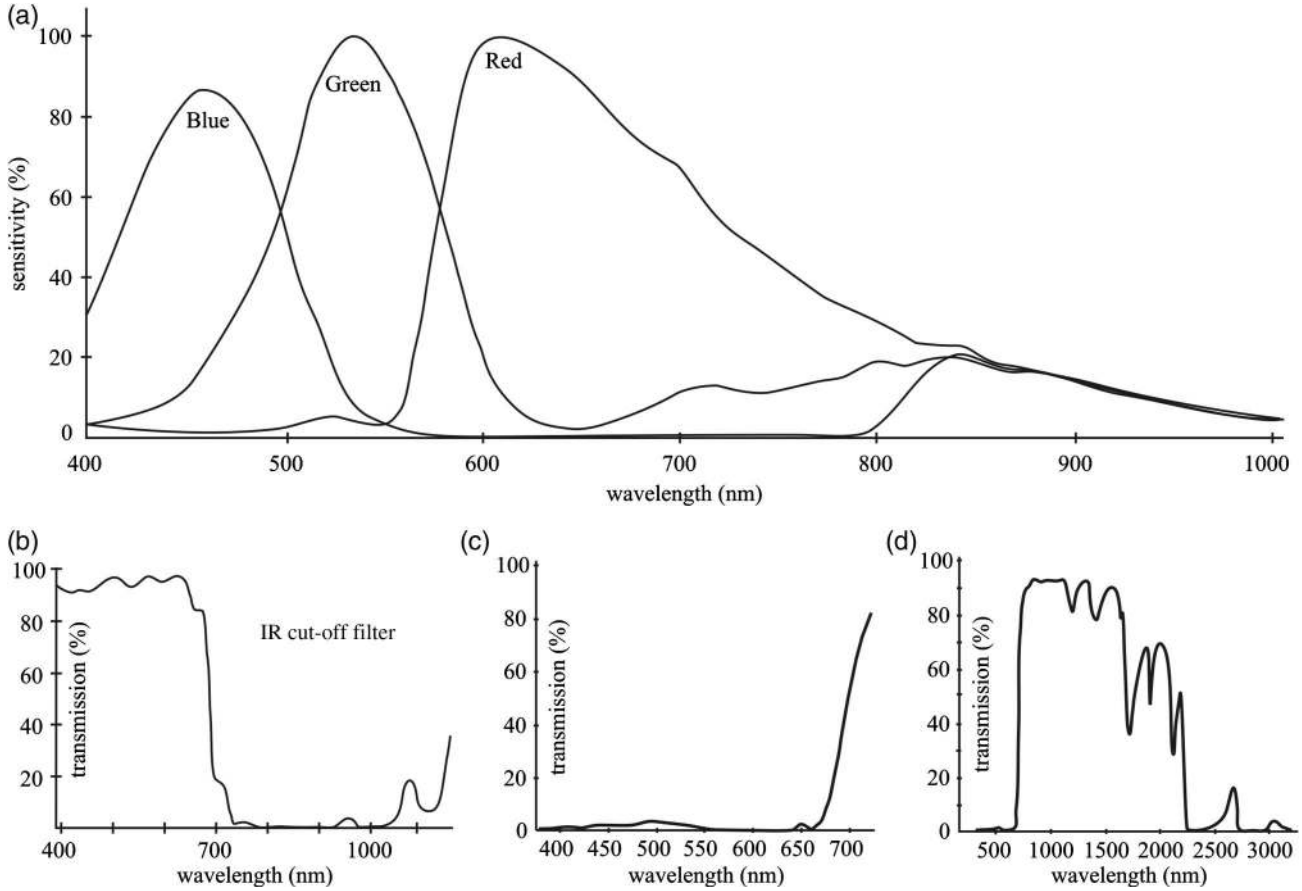

Fig. 3. (a) Sensitivity spectra of the CCD sensor used in our imaging polarimetric cloud detector. The red channel had a sufficiently high sensitivity even in the 700 nm $< \lambda <$ 830 nm range to take measurements in the near-infrared part of the spectrum. (b) Transmission spectrum of the infrared (IR) cut-off filter used for visible imaging. The filter efficiently cut off wavelengths above 700 nm. (c), (d) Transmission spectrum of the visible cut-off filter used for near-infrared imaging. (c) Visible part and (d) the extended infrared part of the transmission spectrum of the filter. The filter efficiently cuts off wavelengths below 650 nm allowing near-infrared measurements.

A custom-made filter wheel was installed between the CCD sensor and the fisheye lens, which was rotated by a servomotor, allowing fast positioning of five different filters. The properties of the filters are listed in Table 1. For visible measurements, we used an infrared cut-off filter, the transmission spectrum of which is shown in Fig. 3(b). For near-infrared measurements, on the other hand, we used a visible cut-off filter with a transmission spectrum, as shown in Figs. 3(c) and 3(d). Although the instrument was also able to take near-infrared images, they were not used in this study.

Table 1. Five Filters Used in the Built-In Rotating Filter Wheel of Our Imaging Polarimetric Cloud Detector[a]

No.	Filter
1	Visible: infrared cut-off filter
2	Infrared: visible cut-off filter
3	Visible polarized: infrared cut-off and visible polarizer filters with 0° transmission angle
4	Visible polarized: infrared cut-off and visible polarizer filters with 45° transmission angle
5	Visible polarized: infrared cut-off and visible polarizer filters with 90° transmission angle

[a]For calibration, we used a visible (optical) filter. Infrared measurements were strictly experimental.

A custom-made sun shield, mounted to the end of an arm in front of the lens, moved a black disk along two axes (azimuth and elevation). The disk could be positioned to shield the whole lens from direct sunlight, which can cause flares due to internal reflections between the lens surfaces and, thus, lead to artifacts in the evaluation of the measurements. The sun shield was moved by servomotors, allowing accurate and fast repositioning to account for ship movements.

A custom-made controller with an embedded computer was responsible for scheduling the observations, positioning the sun shield, controlling the filter wheel, triggering the camera, and storing the images. The computer was managed through a standard TCP/IP connection for configuration, maintenance, and downloading the acquired images.

The entire system was protected from the elements by a robust weatherproof Peli 1650 case. The cover of the case was cut out in order to mount a 42 cm diameter acrylic dome, large enough to allow free movement of the sun shield. The interface between the case and the dome was sealed, and the internal

atmosphere was controlled by a Peltier-element-based cooler and a low-wattage heater foil, with humidity kept low using 1 kg of silica gel.

In certain figures (e.g., Fig. 4), a ghost image of clouds can be seen. This was the consequence of cloud motion during the sequential acquisition of the three linearly polarized photos needed for imaging polarimetry. The tilting of the vessel in heavy seas could further increase this ghosting/blurring. Such motion artifacts can also be seen in a few computed polarization patterns; for example, in the degree of polarization shown in Fig. 4, clouds appear with darker contours. Eliminating such motion effects requires the near simultaneous acquisition of the three photos, which will be achieved using three separate cameras with fixed polarizers [5] in a future improved version of our system. For further comments on the possibility of eliminating motion effects with the help of ship attitude data, see the Discussion.

A few images also showed a so-called smear effect: narrow overexposed stripes due to saturated pixels.

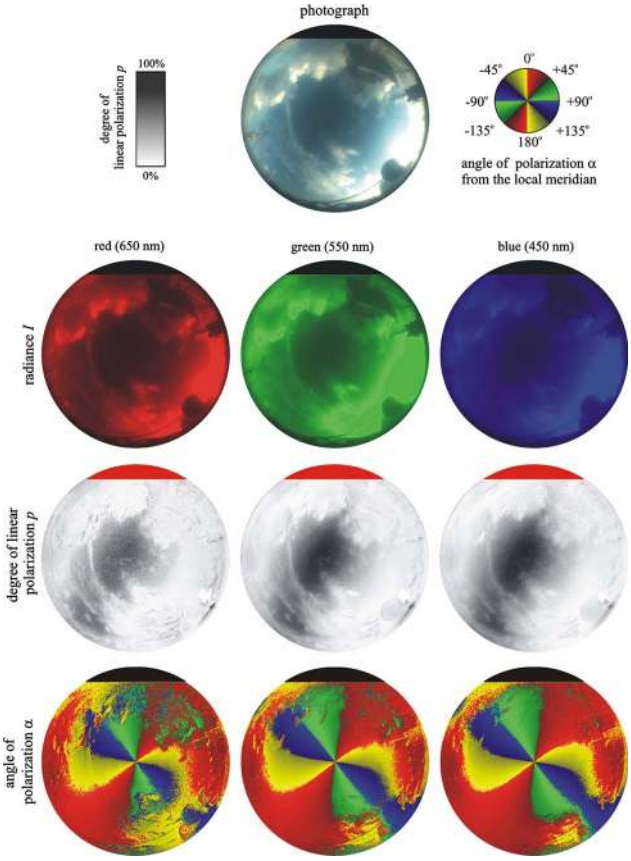

Fig. 4. Results of one of the 50 sky-polarimetric measurements used for training, optimizing, and testing the 13 different cloud detection algorithms. This particular measurement was performed at a low solar elevation angle of 10° and relative cloudiness of 61%, according to the consensus cloud mask. The observation tower, chimney, and upper-deck railings of the *Polarstern* obscured part of the sky. The optical axis of the fisheye lens and the center of the CCD were slightly misaligned, leading to loss of data in the minor segment (black/red area) at the top of each circular image.

This was caused by the architecture of the employed CCD sensor and can be eliminated using a CMOS sensor instead, which does not suffer from such artifacts. Prior experience indicates that our imaging polarimetric technique is able to measure the degree and the angle of skylight polarization with an accuracy of ±1% and ±1°, respectively [5–13,15,21–23]. However, because of the drawbacks of our cloud detector (poor-quality polarization filter, sequential capture of the polarization images on a moving platform), the accuracy was slightly smaller (about ±1–3% and ±1–3°).

In a pilot measurement, we determined the effect of the used acrylic dome on the measured skylight polarization. The effect of the acrylic material turned out to be an order of magnitude smaller than that of dust, raindrops, and sea salt crystals that unavoidably contaminated the dome during the field measurements. Therefore, we concluded that it was unnecessary to further characterize the negligible polarization effect of the acrylic dome, which, otherwise, had excellent optical quality.

C. Testing Method

We selected 50 polarization images for evaluation from the large number of measurements taken during the *Polarstern* expedition (e.g., Fig. 4). The test data set was compiled to represent sky condition diversity as much as possible. Therefore, we prescreened the images to avoid duplicating similar sky conditions; otherwise, data selection was random. This prescreening did not bias the results toward one or another algorithm. A static background mask was created to block out pixels corresponding to the ship's superstructure. For each selected image, three independent cloud masks were then derived by three human observers, based exclusively on the visible color and intensity information, that is, without using near-infrared and polarization information. In the final consensus cloud mask, which was considered the "truth," a pixel was cloudy if at least two observers classified it as such; otherwise, it was clear sky. The error in a human observer's cloud detection was defined as the number of pixels for which the observer's classification disagreed with the consensus divided by the total number of sky pixels outside the static background mask and averaged for the 50 measurements. The 50 selected images were randomly divided into two groups of 25 images to form a training set and a test set. Using the training set, we determined the optimal value of the tunable parameters for the 13 cloud detection algorithms described below and then evaluated the performance of the optimized algorithms on the test set. To characterize the accuracy of an algorithm, we counted the total number N_t of pixels in the test set, excluding the background and the total number N_e of pixels erroneously classified compared with the consensus cloud mask. The error E of an algorithm was then defined as $E = N_e/N_t$. To increase the statistical significance of our results, the calculations

were repeated for 10 different, randomly chosen training set–test set combinations.

D. Cloud Detection Algorithms

We developed several different cloud detection algorithms (or "detectors"), some of which are based solely on photometric information (color images), while others are based on combined photometric and polarimetric information. In addition to our novel algorithms, we implemented standard algorithms recently published in the literature, such as the well-known red–blue ratio (RBR) method [3,24]. On board the *Polarstern*, there was also a simple photometric full-sky cloud imager, which used the RBR algorithm. Generally, we tried several variants of every algorithm, but only the best-performing one was incorporated into the present work. In total, 13 cloud detectors were tested, which are summarized below.

1. *Red-Blue Difference*

The red-blue difference (RBD) detector uses the red (I_R) and blue (I_B) intensity and classifies a pixel as clear sky if the difference $I_R - I_B < c_{rbd}$ and as a cloud, otherwise, where c_{rbd} is a threshold parameter [25]. Clear sky is typically blue, leading to negative difference values, while clouds are typically white/gray or reddish, resulting in near-zero or slightly positive differences.

2. *Whiteness Detector*

The whiteness detector (WD) [9] classifies a pixel as a cloud if it is white/gray and as clear sky, otherwise. A pixel is considered white/gray if $1 - I_R/I_B < c_w$ and $1 - I_G/I_B < c_w$, where I_R, I_G, and I_B are the red, green, and blue intensities, and c_w is a tunable parameter. In our experience, the conditions $I_R < I_B$ and $I_G < I_B$ were always satisfied for the full sky; hence, the values of $1 - I_R/I_B$ and $1 - I_G/I_B$ were always positive.

3. *Red-Blue Ratio*

Similar to RBD, the red-blue ratio (RBR) detector [3,24] also uses the red (I_R) and blue (I_B) intensity and classifies a pixel as clear sky if the ratio $I_R/I_B < c_{rbr}$ and as clouds, otherwise, where c_{rbr} is a tunable parameter. Clear sky is typically blue, leading to smaller ratios, while clouds are typically white/gray or reddish, leading to larger ratios.

4. *k-Nearest Neighbors*

The above algorithms with one or two control parameters share a common weakness in that they only allow limited fine-tuning of cloud detection. To overcome this issue, we implemented the k-nearest neighbors (kNN) algorithm, which is capable of supervised learning. Note that the kNN algorithm was previously used for cloud type classification [25]. During the training process, we created a $256 \times 256 \times 256$ color cube array initialized to zero. Then each pixel in the training set was assigned to a cell in this color cube based on the three measured intensities (I_R, I_G, and I_B), and the cell counter was increased by 1 if the pixel was cloudy and decreased by 1 if it was clear sky (see Section 2.C). Finally, for every pixel in the test set, we determined the corresponding color cube cell and its kNN that had nonzero count values, where k is a tunable parameter. Distances in the array were calculated by the 3D Euclidean formula. A tested pixel was classified as cloudy if there were more positive than negative count values among the neighboring cells and as clear sky, otherwise. In essence, this procedure determined whether a given (RGB) color was more likely to be associated with clouds or clear sky.

5. *Whiteness Detector with Average Intensity*

The whiteness detector with average intensity (WDAI), which we developed, is a variant of the WD, where the threshold value $c_I(I)$ is not constant but varies as a function of the intensity of the median-filtered neighborhood of the investigated pixel. First, the median-filtered intensity is calculated for each spectral band, using a 135×135 pixel filtering window. This window with a diameter of 40.5° was determined by optimization. Then, the median-filtered spectral-mean intensity of the given pixel is calculated: $I = (I_R + I_G + I_B)/3$. Finally, this spectral-mean intensity is used to calculate the threshold value $c_I(I) = a_I \cdot I + b_I$, where a_I and b_I are tunable control parameters.

For the WDAI, both total intensity and unpolarized intensity were tested, with the latter giving a slightly smaller average cloud detection error. The unpolarized intensity I_{up} of a given pixel is calculated as the product of the total intensity I and the degree of unpolarization $1 - p$: $I_{up} = I \cdot (1 - p)$.

6. *Whiteness Detector with Solar Distance*

The whiteness detector with solar distance (WDSD), which we also developed, is yet another variant of the WD detector similar to the WDAI detector, but, in this case, the threshold parameter $c_d(d)$ is a function of the Euclidean distance d between the investigated pixel and the center of the sun in the image. The threshold value is calculated as $c_d(d) = a_d \cdot d + b_d$, where a_d and b_d are tunable parameters. The rationale behind this algorithm is that, because the sky is brighter near the sun, the WD detector can be improved by making the threshold c_d dependent on distance from the sun. We also tested the algorithm using angular distance on the sky-dome and Manhattan distance on the circular sky image; however, the simple Euclidean distance gave the smallest average cloud detection error.

7. *Hybrid Thresholding Algorithm*

The hybrid thresholding algorithm (HTA) operates on the normalized I_B/I_R ratio [defined as

$(I_B/I_R - 1)/(I_B/I_R + 1)$] using either fixed or minimum cross entropy thresholding [26–28]. The uni- or bimodality of the histogram of the normalized I_B/I_R ratio determines the applicable thresholding, using the magnitude of the standard deviation for selecting the thresholding method. An image containing clouds and clear sky typically has a bimodal normalized I_B/I_R ratio histogram with larger standard deviation, while an image of completely clear or overcast sky has a unimodal histogram with smaller standard deviation. Therefore, the algorithm selects between fixed and minimum cross entropy thresholding based on the magnitude of the histogram standard deviation.

We implemented the HTA algorithm based on [26]. However, while in [26] the near-horizon and near-sun areas were masked out in the sky images, we tested the algorithm on all sky pixels. For the fixed threshold, we used $c_{FIX} = (1/c_{rbr} - 1)/(1/c_{rbr} + 1)$, where c_{rbr} is the optimal parameter of the RBR detector. The parameter to be optimized was the c_{SD} standard deviation threshold value, the magnitude of which determined the thresholding method. If the standard deviation of the normalized I_B/I_R ratio histogram was smaller than c_{SD}, the fixed thresholding, otherwise the minimum cross entropy thresholding was used.

8. *Degree of Polarization Difference in the Green Spectral Range*

The degree of polarization difference in the green spectral range (pDG) detector classifies a sky pixel as cloudy if $p_G - p_{Berry} < c_{pDG}$, where p_G is the degree of linear polarization measured in the green spectral range, p_{Berry} is the degree of polarization calculated from the Berry model of clear-sky polarization [29] for the solar position of the measurement, and c_{pDG} is a tunable threshold. Otherwise, the pixel is clear.

9. *Degree of Polarization Ratio in the Green Spectral Range*

The degree of polarization ratio in the green spectral range (pRG) detector classifies a sky pixel as cloudy if $p_G/p_{Berry} < c_{pRG}$, where p_G and p_{Berry} are the same as for pDG above, and c_{pRG} is a tunable threshold. Otherwise, the pixel is clear.

10. *Neural Network*

A large amount of extra information is encoded in polarimetric measurements, which can be incorporated into an optimal cloud detection algorithm with the lowest possible error. There is local optical information, e.g., the red intensity or the blue degree of polarization of the investigated pixel. In addition, there is global optical information, such as the average intensity in the green channel or the variance of the degree of polarization in the blue channel calculated over the entire image. There is also nonoptical information, such as solar elevation or relative solar azimuth. Some of these additional parameters can be easily taken into account; others are more challenging to incorporate in a cloud detection algorithm. The difficulty is to pin down how a human observer determines whether light originating from a given point of the sky represents a cloud or clear sky. It is even possible that a human observer perceives light with certain optical properties as a cloud in one particular situation but as clear sky in another.

To overcome some of these issues, in [4] a multilayer perceptron neural network (NN) was implemented, which is capable of supervised learning but limiting input data to local optical, nonpolarimetric information. The authors' aim was to find an optimal balance between accuracy and speed. Prompted by their results, we also implemented a multilayer perceptron NN with the sigmoid activation function $S(x) = 1/(1 + e^{-x})$. To avoid the possibility of omitting potentially important input information that the neural network could utilize during training, we decided to use as many input parameters as possible. However, investigating whether each input parameter was, in fact, utilized by the trained neural network is beyond the scope of this paper.

The structure of our NN can be characterized by the number of perceptrons in each layer. For example, a network characterized by $i - j - k - 1$ contains i perceptrons in the input layer, j perceptrons in the first internal layer, k perceptrons in the second internal layer, and one perceptron in the output layer. The input layer and every internal layer also contained one extra perceptron, the so-called bias perceptron, which did not connect to the previous layer and always had an output value of 1. The output layer contained only one perceptron, the target output value of which was 0 for clear sky and 1 for cloud. During evaluation, the investigated pixel was classified as clear sky if the output value of the output perceptron was <0.5 and cloudy otherwise. We implemented backpropagation in the learning algorithm with a learning rate of 0.001 to avoid oscillation in the input weights of the perceptrons. Each layer was fully connected to the previous one. The input parameters used are summarized in Table 2. Average and variance of intensity I and degree of polarization p of a given pixel were calculated using a 3×3 pixels window around the given pixel. The simple intensity neural network (SINN) and the simple degree of polarization neural network (SpNN) were characterized by a layer structure of 7-3-1. The layer structure of the complex nonpolarimetric neural network (NNN) was 15-16-16-16-1, while that of the polarimetric neural network (PNN) was 27-28-14-1.

E. Image Quality

The transportable polarimetric cloud detector built specifically for the *Polarstern* expedition necessitated the use of a rugged polarizer system, which was of somewhat lower quality than that used in our land-based instrument [5–12] and, thus, made the

Table 2. Input Parameters Used by Our Four Neural-Network-Based Cloud Detection Algorithms[a]

Input Parameter	PNN	NNN	SINN	SpNN
Average I in the red for the whole image	×	×		
Average I in the green for the whole image	×	×		
Average I in the blue for the whole image	×	×		
Variance of I in the red for the whole image	×	×		
Variance of I in the green for the whole image	×	×		
Variance of I in the blue for the whole image	×	×		
Average p in the red for the whole image	×			
Average p in the green for the whole image	×			
Average p in the blue for the whole image	×			
Variance of p in the red for the whole image	×			
Variance of p in the green for the whole image	×			
Variance of p in the blue for the whole image	×			
Solar elevation	×	×	×	×
Average I in the red for the given pixel	×	×	×	
Average I in the green for the given pixel	×	×	×	
Average I in the blue for the given pixel	×	×	×	
Variance of I in the red for the given pixel	×	×		
Variance of I in the green for the given pixel	×	×		
Variance of I in the blue for the given pixel	×	×		
Average p in the red for the given pixel	×			×
Average p in the green for the given pixel	×			×
Average p in the blue for the given pixel	×			×
Variance of p in the red for the given pixel	×			
Variance of p in the green for the given pixel	×			
Variance of p in the blue for the given pixel	×			
Elevation of the given pixel	×	×	×	×
Azimuth distance of sun and the given pixel	×	×	×	×

[a] I: intensity, p: degree of linear polarization. Parameter usage in the PNN, NNN, SINN, and SpNN neural networks is marked with ×.

images slightly blurry (Fig. 4). We did not employ a spectrally neutral (white or gray) reflective target for white balance calibration either, due to the practical difficulties posed by operating on board a vessel. The lack of continuous white balance calibration additionally turned the sky images slightly bluish. The measurements, however, could still be used in our comparison, because the input data were the same for all implemented cloud detection algorithms, and the algorithm parameters were optimized for these images. Consequently, none of the algorithms had a distinct advantage or disadvantage because of the slight blurriness and bluish tint of the input images.

3. Results

Some of the 50 selected sky scenes were overcast, and some had <100% cloud cover with thick water clouds. The least-cloudy case had about 20% cloudiness. Here, we present one partly cloudy scene as an example of sky-polarimetric measurements used for training, optimizing, and testing the different cloud detection algorithms (Figs. 4 and 5).

Figure 4 shows the patterns of intensity I, degree of linear polarization p, and angle of polarization α in the red (650 nm), green (550 nm), and blue (450 nm) spectral channels. As shown, at a low solar elevation of 10°, the degree of polarization was high ($p > 50\%$) in a wide band passing through the zenith perpendicular to the solar–antisolar meridian, which was generally in the blue clear-sky regions. In contrast, the light from clouds was only weakly polarized ($p < 10\%$). The distribution of the angle of polarization was mirror symmetrical to the solar–antisolar meridian, independently of wavelength. These highly consistent α patterns were only slightly disturbed by clouds.

Figure 5 gives an example for cloud detection results obtained with the use of the intensity and polarization patterns in Fig. 4. Figure 5(a) is the color image of the sky (same as in Fig. 4), and Fig. 5(b) is the corresponding consensus cloud mask derived by the three human observers. Figure 5(c) represents the cloud mask obtained with the overall best PNN algorithm, while Fig. 5(d) shows its comparison to the reference consensus cloud mask. Here, gray, blue, and yellow refer to correctly classified pixels, false negative, and false positive cloud detection, respectively.

Figure 6 shows the I, p, and α patterns in the red, green, and blue channels of an almost overcast sky with a cloudiness of 96%, observed at a solar elevation of 16°. The polarization characteristics of overcast skies are qualitatively similar to those of partly cloudy skies (cf. Fig. 4). The main difference is that the degree of polarization from overcast skies is strongly reduced in the entire sky-dome (Fig. 6). Most remarkably, at a given solar elevation, the α pattern of partly cloudy (Fig. 4) and overcast (Fig. 6) skies is practically the same as that of clear skies (see, e.g., the clear-sky figures in [5–12]), independent of wavelength.

The fraction of erroneously classified pixels averaged over the 10 randomly chosen test sets is summarized in Table 3 for the 13 evaluated algorithms. The RBD, HTA, RBR, WD, WDAI, WDSD, and kNN algorithms had similar average errors

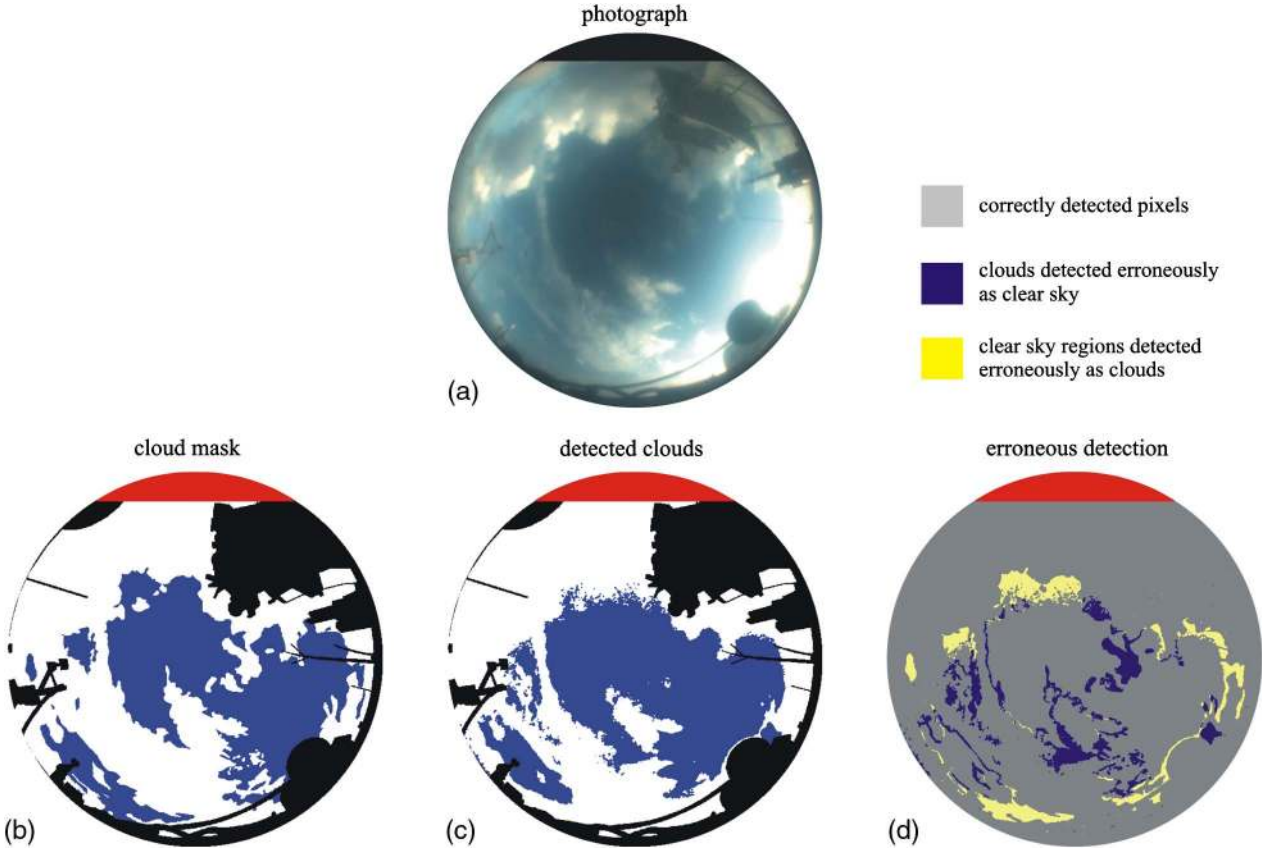

Fig. 5. Example cloud detection results obtained using the intensity and polarization patterns in Fig. 4. (a) Color image of the sky. (b) Consensus cloud mask derived by three human observers. (c) Cloud mask obtained with the PNN algorithm. (d) Differences between the consensus cloud mask and the PNN cloud mask. Gray: correctly classified pixels. Blue: false negative cloud detection. Yellow: false positive cloud detection.

ranging from 18.57% to 22.58%. The pRG and pDG algorithms, which are based only on the degree of polarization, were the least accurate with errors varying between 29.94% and 42.88%. The neural-network-based SpNN algorithm, which uses the degree of polarization, had an error of 23.82% and, thus, provided no improvement over the non-neural-network-based methods. The SINN and NNN neural network algorithms, which use no polarization data, however, performed better than the non-neural-network-based algorithms, having errors between 16.05% and 16.32%. The error of the PNN algorithm, which uses all possible data (polarization, global, and nonoptical), was the smallest (15.32%) among the investigated schemes. The error of WDSD had the smallest standard deviation of SD = 1.00%, while pDG and pRG had the largest SD of 2.69% and 2.35%. The other algorithms had an SD ranging between 1.09% and 1.61%.

The errors of the three human-observer-derived cloud masks compared to the consensus cloud mask (i.e., the percentage of pixels for which a given observer disagreed with the group consensus; see Materials and Methods) were 3.32%, 3.31%, and 2.74%, averaged over the 50 test images. Note that 90% of all pixels were consistently classified by all three observers and 93% by any two observers.

The fraction of erroneously classified pixels calculated separately for each of the 10 random test sets is given in Table 4. As shown, the neural-network-based algorithms outperformed the non-neural-network-based ones not only on average, but also for each individual test set.

The HTA, NNN, and PNN algorithms use global parameters that are characteristic of the whole image, while the WDSD, SINN, SpNN, NNN, and PNN algorithms also use nonoptical parameters such as solar elevation and relative solar azimuth (see Table 2). The comparison statistics in Table 3 reveal that the WDSD algorithm had the smallest error among the non-neural-network-based algorithms, indicating that nonoptical parameters can improve cloud detection. Overall, the NNN and PNN algorithms had the smallest errors, the reason for which is explained in the Discussion section.

4. Discussion

Tables 3 and 4 lack the comparison of cloud detection accuracies of the investigated algorithms to that of a human observer. Although there was a qualified meteorologist on board the *Polarstern*, he did not make cloud coverage observations at the points of time of our measurements. Note, that these human observations of cloud coverage expressed in octas

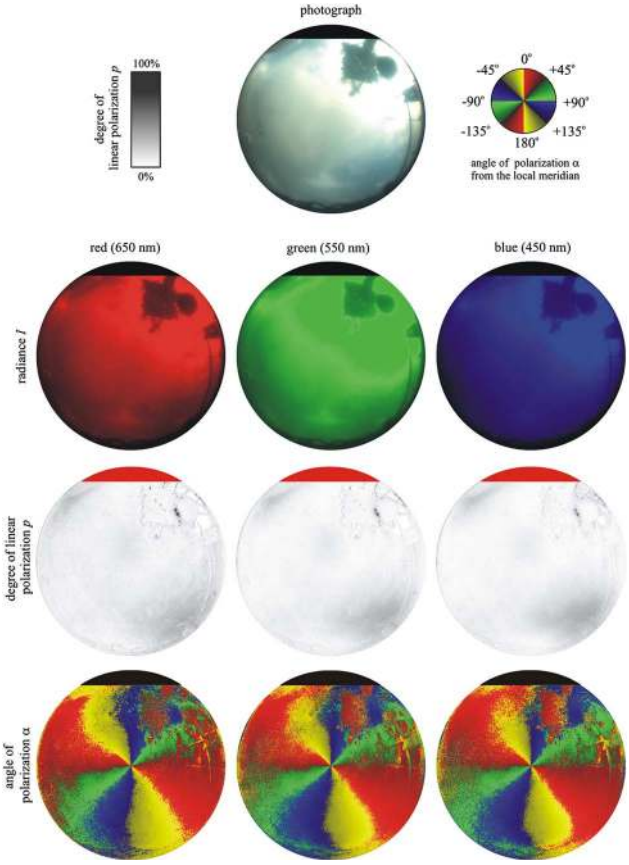

Fig. 6. Same as Fig. 4 but for an almost overcast sky with a relative cloudiness of 96%, according to the consensus cloud mask, observed at a solar elevation angle of 16°.

(1/8th area of the total sky) have a coarse scale resolution compared to that of the investigated algorithms. Furthermore, *Polarstern* was equipped with numerous weather sensors (LIDAR, radiometers, for example) performing regular and frequent measurements, but none of these sensors measured cloud coverage.

The *k*NN, SINN, S*p*NN, NNN, and PNN algorithms belong to the family of artificial intelligence (AI) methods, which are capable of incorporating otherwise difficult to explore relationships. The non-AI algorithms (RBD, RBR, HTA, WD, WDAI, WDSD, *p*DG, *p*RG) might reproduce relationships a human expert can discover by analyzing cloud images, but they are unable to capture hidden relationships, especially those related to polarization properties invisible to the human eye.

However, supervised learning methods are most effective when trained on a sufficiently large number of input data. For example, Tables 3 and 4 clearly show that, although *k*NN is an AI algorithm, its errors were similar to those of the non-AI algorithms. This was the consequence of our specific implementation of *k*NN using only the three intensities (I_R, I_G, I_B; i.e., color) as input. The number of *k*NN input parameters in our study was limited by the large memory requirement of storing the algorithm's internal parameters. In the tested case, we used an array of $256 \times 256 \times 256$ color cells, requiring a modest 16 MB of memory at 1 byte per cell. However, the number of data cells and thus the amount of memory needed to run the *k*NN algorithm rapidly increases with the number n of input parameters as 256^n. For example, if one more parameter were included in the *k*NN algorithm (e.g., the red degree of polarization or the blue angle of polarization), the 4 GB of extra memory required would consume the entire memory of a typical low-end notebook computer used in portable full-sky imaging systems (like our cloud detector).

Table 3. Fractional Error (%) for Each Algorithm of the Erroneously Classified Pixels Averaged over 10 Randomly Chosen Test Sets[a]

Algorithm (Detector)	Average Error (%)	Standard Deviation (%)	Using		
			Polarization Data	Global Parameters	Nonoptical Parameters
RBD	22.58	1.40			
WD	21.46	1.45			
RBR	21.64	1.41			
kNN	19.63	1.14			
HTA	20.78	1.61		×	
WDAI	19.80	1.21			
WDSD	18.57	1.00			×
*p*DG	42.88	2.69	×		
*p*RG	29.94	2.35	×		
S*p*NN	23.82	1.15	×		×
SINN	16.32	1.12			×
NNN	16.05	1.24		×	×
PNN	15.32	1.09	×	×	×

[a]RBD, red-blue difference; WD, whiteness detector; RBR, red-blue ratio; *k*NN, *k*-nearest neighbors; HTA, hybrid thresholding algorithm; WDAI, whiteness detector with average intensity; *p*DG, degree of polarization difference in the green spectral range; *p*RG, degree of polarization ratio in the green spectral range; WDSD, whiteness detector with solar distance; SINN, simple intensity neural network; S*p*NN, simple degree of polarization neural network; NNN, nonpolarimetric neural network; PNN, polarimetric neural network. The 10 sets of 25 test images were randomly chosen from the same pool of 50 images obtained during the ANT-XXVII/1 trans-Atlantic expedition of the research vessel *Polarstern*. The usage of polarization information, global parameters, and nonoptical parameters in the 13 different cloud detection algorithms is marked with ×.

Table 4. Fractional Error (%) of the 13 Different Cloud Detection Algorithms Separately for the 10 Different Randomly Chosen Test Sets[a]

No.	RBD	WD	RBR	*k*NN	HTA	WDAI	WDSD	*p*DG	*p*RG	S*p*NN	SINN	NNN	PNN
1	23.01	20.37	20.61	19.37	19.35	19.43	18.24	38.77	27.33	22.93	16.04	16.03	***15.71***
2	23.69	24.01	24.24	21.25	23.05	21.73	20.16	47.94	32.84	25.19	17.98	18.46	***15.56***
3	21.88	20.06	20.40	18.34	19.06	18.68	17.92	41.51	27.71	22.43	15.21	14.95	***13.47***
4	24.05	22.76	22.93	20.76	22.56	21.05	19.39	43.64	32.22	24.61	17.89	16.85	***16.52***
5	20.89	21.85	22.02	19.38	20.94	19.65	18.28	44.20	29.48	23.26	15.77	***15.40***	15.54
6	24.95	22.36	22.31	21.06	21.94	21.12	19.96	42.14	30.69	25.26	17.51	17.19	***16.42***
7	22.29	19.39	19.58	18.46	18.39	18.60	17.95	39.95	28.14	22.79	15.70	***14.34***	15.01
8	21.55	20.30	20.58	18.18	20.19	18.68	17.22	41.88	27.79	23.24	15.84	15.05	***14.23***
9	20.59	21.11	21.18	19.28	20.08	18.59	17.58	43.09	29.31	23.15	14.79	15.64	***14.13***
10	22.92	22.35	22.54	20.16	22.19	20.52	18.95	45.73	33.86	25.38	***16.46***	16.59	16.59
AV	22.58	21.46	21.64	19.63	20.78	19.80	18.57	42.88	29.94	23.82	16.32	16.05	***15.32***
SD	1.40	1.45	1.41	1.14	1.61	1.21	1.00	2.69	2.35	1.15	1.12	1.24	1.09

[a]The average (AV) and standard deviation (SD) of the errors over the 10 test cases shown in the last two rows are from Table 3. RBD, red-blue difference; WD, whiteness detector; RBR, red-blue ratio; *k*NN, *k*-nearest neighbors; HTA, hybrid thresholding algorithm; WDAI, whiteness detector with average intensity; *p*DG, degree of polarization difference in the green spectral range; *p*RG, degree of polarization ratio in the green spectral range; WDSD, whiteness detector with solar distance; SINN, simple intensity neural network; S*p*NN, simple degree of polarization neural network; NNN, nonpolarimetric neural network; PNN, polarimetric neural network. For each test set as well as for the average, the smallest fractional error of the best algorithm is bolded and italicized.

The *p*DG, *p*RG, S*p*NN, and PNN algorithms use polarimetric information, while the others only use photometric information. The HTA, NNN, and PNN algorithms also use global parameters characteristic of the entire image, whereas the others only use local parameters characteristic of the investigated pixel or its vicinity. The WDSD, S*p*NN, SINN, NNN, and PNN algorithms incorporate nonoptical parameters as well, while the others only utilize optical parameters. The NNN and PNN algorithms produced the smallest errors (see Table 3) because they are AI-based and use a large number of input parameters, including nonoptical and global parameters. The PNN algorithm even uses polarimetric input parameters, which can explain why it slightly outperformed the NNN algorithm.

The difference between the performance of the PNN and NNN algorithms was small and could be insignificant. Nevertheless, the somewhat better performance of PNN over NNN is ultimately not surprising because the former uses more information. This expectation is reflected in the results without any artificial manipulation of the measurement data or the evaluation process. Furthermore, we used as many as 50 cloud scenes for evaluation to reduce the chance of an overall poorly performing algorithm being well optimized to a specific set of sky conditions and, thus, returning unrepresentatively good results. As NNN and PNN used identical measurements with the same bluish ghosting artifacts, image quality cannot explain the better performance of PNN over NNN.

Admittedly, the limited number of training images could not guarantee that the training phase space of the neural network (NN) encompassed all possible cloud scenarios. However, if a test measurement were indeed outside the training phase space, this would weaken the performance of the NN. Thus, our results do not overestimate the accuracy of NN.

We would like to emphasize that cloud detection algorithms more complex than the ones presented in this work might show better performance. While the algorithms in our study were quite diverse, we restricted ourselves to only 13 of them. It is possible that certain combinations of these algorithms could lead to more precise cloud detection. Examining the effectiveness of each algorithm as a function of sun-view geometry and proximity to the horizon, for example, might tell us how to construct improved algorithms that combine several methods but with different weights in different regions of the sky. Our aim was to evaluate several non-neural-network-based algorithms that imitate the process of a human observer detecting clouds in the sky or its measured polarization patterns. In addition, we implemented the neural-network-based PNN algorithm, which incorporates as much information as possible in a way that the dependence of the output on the input parameters is not predetermined.

During our voyage, very high solar elevations with the sun close to the zenith were rare. Even around the equator, the sun only approached the zenith at noon. However, at very high solar elevations, the sky was usually too cloud-free anyway to test the cloud detection algorithms. When the sun is near the zenith, the celestial patterns of the degree and angle of polarization significantly differ from those for low solar elevations; thus, specially trained cloud detection algorithms might be needed. Because the solar elevation angle varied between 4° and 40° in our cloudy images, we could not study this special situation, the investigation of which could be the task of future research. On the basis of our earlier experience [5–13,15,21–23], the mask due to the sun occultor and the field objects of the research vessel *Polarstern* screened out a larger net sky area than the celestial regions of clear skies detected erroneously as cloudy. Therefore, in the test set we omitted clear sky pictures, which, however, did not affect the development of cloud detection algorithms.

The angle of skylight polarization α cannot practically be used for cloud detection because its celestial

pattern is very robust, even under cloudy conditions [6,8–12,21,23]. In [5], a cloud detection algorithm was presented, which also takes into consideration the α of skylight. However, using only changes in α for cloud detection would yield poor results; thus, our cloud detection algorithms did not use this parameter.

The moving platform of the *Polarstern* had the drawback in that the sequential measurements with our rotating-analyzer imaging polarimeter could lead to motion artifacts caused by the varying tilt of the vessel during acquisition of the three polarization pictures. The quality of a few measurements was, in fact, degraded by the ship's movement. However, during selection of the 50 test images, we paid special attention to avoid measurements with apparent motion artifacts in the calculated polarimetric parameters. In theory, these motion artifacts could be eliminated using three simultaneously taken polarization images of the cloudy sky [5]. In practice, however, such an approach would still face the following nontrivial technical challenges: (1) the most serious problem is the proper parallel alignment of the optical axes of the three cameras, which would require an extra collocation step; (2) another difficulty is posed by the slight differences among the photometric (intensity) responses of the three sensors even if they are of the same type, requiring cross calibration. One could also use the ship's motion and attitude data to correct the currently available measurements by computing an offset position for each pixel and sequential image. However, we deemed this approach too involved which would have needed an accurate and complex temporal synchronization among ship motion, ship attitude, and acquisition time of the polarization images. Instead, we applied the simpler method of using a sequential one-camera rotating-analyzer polarimeter but with measurements affected by motion artifacts excluded from analysis.

5. Conclusions

We found that neural-network-based algorithms perform the best among the investigated schemes and also that global image properties (e.g., the mean and variance of intensity), nonoptical information (e.g., sun-view geometry), and polarimetric information (especially the degree of polarization) can improve the accuracy of cloud detection. However, as evidenced by the rather small increase in accuracy between the NNN and PNN detectors, the addition of polarimetric information only marginally improves cloud detection. Nevertheless, it is important to emphasize that polarization information can be used to derive other quantities such as cloud base height or aerosol concentration [30], which would be impossible to measure by a photometric sky imager alone. Polarization might also be helpful in classifying cloud types, e.g., distinguishing ice clouds from water clouds, or even obtaining information on ice cloud microphysics (particle size and shape).

We would like to thank the German Alfred Wegener Institute for the opportunity to participate in the ANT-XXVII/1 expedition aboard the research vessel *Polarstern*. This work was supported by the grant OTKA K-105054 (Full-Sky Imaging Polarimetry to Detect Clouds and to Study the Meteorological Conditions Favourable for Polarimetric Viking Navigation) received by Gábor Horváth from the Hungarian Science Foundation. Gábor Horváth also thanks the German Alexander von Humboldt Foundation for an equipment donation and a three-month research fellowship (3.3-UNG/1073032 STP) from 1 June to 31 August 2013 at the University of Regensburg). We are grateful to four anonymous reviewers for their valuable and constructive comments.

References

1. J. Kalisch and A. Macke, "Estimation of the total cloud cover with high temporal resolution and parametrization of short-term fluctuations of sea surface insolation," Meteorologische Zeitschrift **17**, 603–611 (2008).
2. C. W. Chow, B. Urquhart, M. Lave, A. Dominguez, J. Kleissl, J. Shields, and B. Washom, "Intra-hour forecasting with a total sky imager at the UC San Diego solar energy testbed," Solar Energy **85**, 2881–2893 (2011).
3. A. Ohmura, E. G. Dutton, B. Forgan, C. Fröhlich, H. Gilgen, H. Hegner, A. Heimo, G. König-Langlo, B. McArthur, G. Müller, R. Philipona, R. Pinker, C. H. Whitlock, K. Dehne, and M. Wild, "Baseline Surface Radiation Network (BSRN/WCRP): new precision radiometry for climate research," Bull. Am. Meteorol. Soc. **79**, 2115–2136 (1998).
4. A. Cazorla, F. Olmo, and L. Alados-Arboledas, "Development of a sky imager for cloud cover assessment," J. Opt. Soc. Am. A **25**, 29–39 (2008).
5. G. Horváth, A. Barta, J. Gál, B. Suhai, and O. Haiman, "Ground-based full-sky imaging polarimetry of rapidly changing skies and its use for polarimetric cloud detection," Appl. Opt. **41**, 543–559 (2002).
6. R. Hegedüs, S. Åkesson, and G. Horváth, "Polarization patterns of thick clouds: overcast skies have distribution of the angle of polarization similar to that of clear skies," J. Opt. Soc. Am. A **24**, 2347–2356 (2007).
7. J. Gál, G. Horváth, A. Barta, and R. Wehner, "Polarization of the moonlit clear night sky measured by full-sky imaging polarimetry at full moon: comparison of the polarization of moonlit and sunlit skies," J. Geophys. Res. D **106**, 22647–22653 (2001).
8. B. Suhai and G. Horváth, "How well does the Rayleigh model describe the E-vector distribution of skylight in clear and cloudy conditions? A full-sky polarimetric study," J. Opt. Soc. Am. A **21**, 1669–1676 (2004).
9. I. Pomozi, G. Horváth, and R. Wehner, "How the clear-sky angle of polarization pattern continues underneath clouds: full-sky measurements and implications for animal orientation," J. Exp. Biol. **204**, 2933–2942 (2001).
10. R. Hegedüs, S. Åkesson, R. Wehner, and G. Horváth, "Could Vikings have navigated under foggy and cloudy conditions by skylight polarization? On the atmospheric optical prerequisites of polarimetric Viking navigation under foggy and cloudy skies," Proc. R. Soc. A **463**, 1081–1095 (2007).
11. R. Hegedüs, S. Åkesson, and G. Horváth, "Anomalous celestial polarization caused by forest fire smoke: why do some insects become visually disoriented under smoky skies?" Appl. Opt. **46**, 2717–2726 (2007).
12. R. Hegedüs, A. Barta, B. Bernáth, V. B. Meyer-Rochow, and G. Horváth, "Imaging polarimetry of forest canopies: how the azimuth direction of the sun, occluded by vegetation, can be assessed from the polarization pattern of the sunlit foliage," Appl. Opt. **46**, 6019–6032 (2007).

13. G. Horváth, ed., *Polarized Light and Polarization Vision in Animal Sciences*, Springer Series in Vision Research (Springer, 2014), Vol. **2**.
14. K. L. Coulson, *Polarization and Intensity of Light in the Atmosphere* (Deepak Publishing, 1988).
15. G. Horváth and D. Varjú, *Polarized Light in Animal Vision—Polarization Patterns in Nature* (Springer, 2004).
16. P. Y. Deschamps, F. M. Bréon, M. Leroy, A. Podaire, A. Bricaud, J. C. Buriez, and G. Seze, "The POLDER mission: instrument characteristics and scientific objectives," IEEE Trans. Geosci. Remote Sens. **32**, 598–615 (1994).
17. B. Fougnie, G. Bracco, B. Lafrance, C. Ruffel, O. Hagolle, and C. Tinel, "PARASOL in-flight calibration and performance," Appl. Opt. **46**, 5435–5451 (2007).
18. F. M. Bréon and M. Doutriaux-Boucher, "A comparison of cloud droplet radii measured from space," IEEE Trans. Geosci. Remote Sens. **43**, 1796–1805 (2005).
19. B. Cairns, B. E. Carlson, A. A. Lacis, and E. E. Russell, "An analysis of ground-based polarimetric sky radiance measurements," Proc. SPIE **3121**, 382–393 (1997).
20. K. Bumke, "The expedition of the research vessel Polarstern to the Antarctic in 2010 (ANT-XXVII/1)," K. Bumke, ed. (with contributions of the participants). *Berichte zur Polar- und Meeresforschung* (Reports on Polar and Marine Research), Report No. 628 (2011), pp. 1–82.
21. J. Gál, G. Horváth, V. B. Meyer-Rochow, and R. Wehner, "Polarization patterns of the summer sky and its neutral points measured by full-sky imaging polarimetry in Finnish Lapland north of the Arctic Circle," Proc. R. Soc. A **457**, 1385–1399 (2001).
22. A. Barta, A. Farkas, D. Száz, Á. Egri, P. Barta, J. Kovács, B. Csák, I. Jankovics, G. Szabó, and G. Horváth, "Polarization transition between sunlit and moonlit skies with possible implications for animal orientation and Viking navigation: anomalous celestial twilight polarization at partial moon," Appl. Opt. **53**, 5193–5204 (2014).
23. G. Horváth, A. Barta, I. Pomozi, B. Suhai, R. Hegedüs, S. Åkesson, B. Meyer-Rochow, and R. Wehner, "On the trail of Vikings with polarized skylight: experimental study of the atmospheric optical prerequisites allowing polarimetric navigation by Viking seafarers," Phil. Trans. R. Soc. B **366**, 772–782 (2011).
24. C. Long and J. DeLuisi, "Development of an automated hemispheric sky imager for cloud fraction retrievals," in *Proceedings of the 10th Symposium on Meteorological Observations and Instrumentation*, Phoenix, Arizona, 11 January 1998.
25. A. Heinle, A. Macke, and A. Srivastav, "Automatic cloud classification of whole sky images," Atmos. Meas. Tech. Disc. **3**, 269–299 (2010).
26. Q. Li, W. Lu, and J. Yang, "A hybrid thresholding algorithm for cloud detection on ground-based color images," J. Atmos. Ocean. Technol. **28**, 1286–1296 (2011).
27. C. H. Li and C. Lee, "Minimum cross entropy thresholding," Pattern Recogn. **26**, 617–625 (1993).
28. C. Li and P. Tam, "An iterative algorithm for minimum cross entropy thresholding," Pattern Recogn. Lett. **19**, 771–776 (1998).
29. M. V. Berry, M. R. Dennis, and R. L. Lee, Jr., "Polarization singularities in the clear sky," New J. Phys. **6**, 162 (2004).
30. A. Kreuter and M. Blumthaler, "Feasibility of polarized all-sky imaging for aerosol characterization," Atmos. Meas. Tech. Disc. **5**, 8815–8838 (2012).